Check for updates

Understanding the role of Cu$^+$/Cu^0 sites at Cu$_2$O based catalysts in ethanol production from CO$_2$ electroreduction -A DFT study†

Liren Sun,[a] Jinyu Han,[a] Qingfeng Ge, [b] Xinli Zhu [a] and Hua Wang *[a]

Cu$_2$O based electrocatalysts generally exhibit better selectivity for C$_2$ products (ethylene or ethanol) in electrochemical carbon dioxide reduction. The surface characteristic of the mixed Cu$^+$ and Cu^0 chemical state is believed to play an essential role that is still unclear. In the present study, density functional theory (DFT) calculations have been performed to understand the role of copper chemical states in selective ethanol formation using a partially reduced Cu$_2$O surface model consisting of adjacent Cu$^+$/Cu^0 sites. We mapped out the free energy diagram of the reaction pathway from CO intermediate to ethanol and discussed the relation between the formation of critical reduction intermediates and the configuration of Cu$^+$/Cu^0 sites. The results showed that Cu$^+$ sites facilitate the adsorption and stabilization of *CO, as well as its further hydrogenation to *CHO. More importantly, as compared to the high reaction energy (1.23 eV) of the dimerization of two *CO on Cu$^+$/Cu^0 sites, the preferable formation of *CHO on the Cu$^+$ site makes the C–C coupling reaction with *CO on the Cu^0 site happen under a relatively lower energy barrier of 0.58 eV. Furthermore, the post C–C coupling steps leading to the formation of the key intermediate *OCHCH$_2$ to C$_2$ compound are all thermodynamically favoured. Noteworthily, it is found that *OCHCH$_2$ inclines to the ethanol formation because the coordinatively unsaturated Cu$^+$ site could maintain the C–O bond of *OCHCH$_2$, and the weak binding between *O and Cu$^+$/Cu^0 sites helps inhibit the pathway toward ethylene. These findings may provide guidelines for the design of CO and CO$_2$ reduction active sites with enhanced ethanol selectivity.

1. Introduction

Excessive carbon dioxide emissions have triggered a serious environmental crisis around the world, and have also posed many urgent and irreversible threats to human societies.[1–5] The electrochemical CO$_2$ reduction reaction using renewable power has become an excellent long-term solution.[6] Among various reduction products, ethanol, as a widespread fuel blend and important chemical raw material, is highly valuable and desirable. However, electrochemical conversion of CO$_2$ into multi-carbon (C$_{2+}$) hydrocarbons or oxygenated products faces many challenges.[7]

Among copper-based catalysts, oxide derived Cu catalysts are unique because they reduce CO$_2$ to significant amounts of C$_2$ and higher-order hydrocarbons and alcohols.[6–14] For improving

the C$_2$ product selectivity, the mechanism study of C–C coupling of C$_1$ intermediates and the post C–C coupling steps leading to C$_2$ have received extensive attention. According to our previous study and several experimental studies,[15–17] the kinetics of C–C coupling reactions could be promoted by providing sufficient CO formation using bimetallic Au/Ag–Cu based catalysts.[18,19] That is CO$_2$ could be selectively converted to CO on Au or Ag sites and the formed CO molecules spill over to the nearby Cu sites, where they undergo further C–C coupling reactions and sequential reduction steps to C$_2$ products. Therefore, this suggests that more comprehensive studies are necessary to understand the mechanism of the adsorption and C–C coupling reaction of the intermediate CH$_x$O ($x = 0$–2) on copper active sites, which are crucial to the production of C$_{2+}$ products. At this point, it is the most important to design active sites, which can stabilize the critical intermediate *CO and other C$_1$ intermediates, and catalyse C–C coupling reactions as well as the further reduction reactions of dimers.

It has been reported that catalysts containing adjacent Cu$^+$ and Cu^0 sites are more conducive to forming C$_{2+}$ products compared with the pure Cu catalyst.[20,21] Lee et al. observed that their Cu$_2$O catalyst was only partially reduced, leaving an oxide layer on the top, which means that Cu$^+$ together with Cu^0 obviously remained on the surface.[22] Moreover, this Cu$_2$O-

aCollaborative Innovation Center of Chemical Science and Engineering, Key Laboratory for Green Chemical Technology, School of Chemical Engineering and Technology, Tianjin University, Tianjin, 300350, China. E-mail: tjuwanghua@tju.edu.cn

bDepartment of Chemistry and Biochemistry, Southern Illinois University, Carbondale, Illinois, 62901, USA

† Electronic supplementary information (ESI) available. See https://doi.org/10.1039/d2ra02753d

derived catalyst induced significantly enhanced selectivity on C_2 production. Yang *et al.* synthesized Cu_2O catalysts with nano-cavities to enable the confinement of carbon intermediates generated *in situ*, which stabilizes the Cu^+ species.[23] Their results also lead to the marked C_2 selectivity at a large conversion rate. These studies have aroused extensive interest to explore the effects of mixed copper sites on the C_2 formation.[24,25]

Goddard and co-workers performed a study on a Cu metal embedded in oxidized matrix system (MEOM) having both Cu^0 and Cu^+ on the surface.[26] The results demonstrated that Cu^+ sites, if presented on the Cu surface, would have indeed a strong effect on activating CO_2 and C–C coupling. In contrast to the metal matrix with only Cu^0 and the fully oxidized matrix containing only Cu^+, the improved efficiency and selectivity on MEOM are attributed to the synergistic effect between neighbouring sites Cu^+ and Cu^0 for significantly improving the kinetics and thermodynamics of CO dimerization, whereas their result indicated that the formation of a C–C bond on MEOM exclusively occurs through the dimerization of *CO, rather than *via* the surface bound moieties *CHO or *COH pathway. Meanwhile on experimental basis, Zhang *et al.* built an efficient catalyst $Cu^0@PIL@Cu^I$ consisting of inner Cu^0-PIL and outer PIL-Cu^I to perform a tandem catalysis process. The high selectivity and high reaction rate of C_2+ products were ascribed to the numbers and highly dispersed Cu^0-PIL-Cu^I interfaces.[27] However, the DFT calculation was conducted on the Cu^0-(111) surface without involving the tandem catalytic sites. Moreover, Gong *et al.* obtained a notable enhancement in the CO_2RR by synthesizing the controllable Cu^+–Cu^0 sites on $CuO/CuSiO_3$.[28] And their DFT calculations elucidate that Cu^+ sites strengthen the *CO adsorption and promote CO dimerization. However, many other C–C coupling pathways involving hydrogenated species are not explored.[29] Therefore, much progress has been made in understanding the parameters favouring C_2 *vs.* C_1 products, or understanding the ethylene formation as it dominates the C_2 products. Although some groups have started analysing the energetics of the pathways leading to ethanol, there needs a clear consensus regarding the factors affecting the competition between ethylene and ethanol, and the intermediates where the pathway bifurcates. In addition, a more informative correlation between the presence of Cu^+ species and the ethanol generation has not been well established.[30–32] In this sense, a more precise model simulating the mixed Cu^+/Cu^0 active sites toward the CO_2RR is required to get a deeper insight into the above points.

In this work, density functional theory (DFT) calculations were performed to explore the mechanism on the mixed Cu^+/Cu^0 active sites for ethanol formation in the CO_2RR. A bulk $Cu_{32}O_8$ was obtained by simulating the "oxide-derived" process from Cu_2O in our previous work.[33] The $Cu_{32}O_8$ (100) surface with the adjacent Cu^0 and Cu^+ sites was built as a catalyst model. We examined the stability of possible intermediates formed along the pathways of the CO reduction reaction toward C_2 product and constructed free energy diagrams. We aim to figure out the role of Cu^+/Cu^0 active sites during the CORR, in terms of the adsorption of CO, the energetics of *CO hydrogenation and the involved C_1 intermediates in the critical step of C–C coupling as well. Besides, the later reduction reactions after C–C coupling are also explored for the pathways leading to ethanol. We try to find the key intermediate on the branch determining the pathway to ethanol formation and explore the relation between active sites and ethanol selectivity.

2. Methods and computational details

All calculations were performed using the Vienna *Ab Initio* Simulation Program (VASP) package.[34–37] The periodic DFT code uses the projector-augmented wave (PAW) method to create effective core potentials and plane waves for valence electrons. Due to the strong correlation nature of copper oxide, it is known that the standard DFT methodology fails to reproduce the other electronic structure properties and accurate energetics. We used the DFT + U method and Perdew, Burke, and Ernzerhof (PBE) functional[38] to calculate the exchange-correlation energy. The U_{eff} is the difference between the Coulomb U and exchange J parameters. The effects of U_{eff} values and antiferromagnetic ordering were described in our previous work in detail. According to our calculations, a U_{eff} of 7 eV not only maintained a good prediction of the structural parameters but also improved the prediction of the band gap and magnetic moments of copper oxide, which agreed with a previous study.[39] A cutoff energy of 400 eV was used for the plane wave basis set in our calculations. The convergence criteria for electronic self-consistence were set at 1×10^{-5} eV and for ionic relaxation at 0.01 eV $Å^{-1}$.

The slab model was constructed based on a $Cu_{32}O_8$ bulk reported in our previous work.[33] The lattice parameters of $Cu_{32}O_8$ are $a = 9.10$ Å, $b = 6.06$ Å, and $c = 9.10$ Å. The $Cu_{32}O_8$ structures are allowed to reconstruct by stochastic surface walking global optimization together with the high-dimensional neural network potential (SSW-NN) method. By reproducing the $Cu_{32}O_8$ unit cell in the y direction, the A (1×2) surface unit cell resulted in a supercell. The optimized bulk structure was used to construct the slab model of the $Cu_{32}O_8(100)$ surface. The thickness of the slab model is four layers and each layer consists of Cu and O atoms. The vacuum of the slab model is 10 Å. A $(2 \times 2 \times 1)$ k-point grid was used to sample the surface Brillouin zone. All atomic positions are allowed to change during structural relaxations.

In this work, we adopt the computational hydrogen electrode (CHE) method proposed by Nørskov and co-workers to calculate the free energies of adsorbates for the CO_2 reduction reaction.[40] The proton-coupled electron transfer (PCET) step has a negligible kinetic barrier at room temperature[41] and the step with the most positive energy would be the limiting step.

According to this method, the reference electrode potential of one electron–proton pair equals half molecule of hydrogen gas at the standard pressure $[(H^+ + e^-) \leftrightarrow 1/2H_2(g)]$. The free energy of each intermediate in the reaction at potential $U\,(\neq 0)$ will be shifted by $|e|U$, as shown below, where e is the elementary charge and U is the electrode potential.

$$\Delta G_n(U) = \Delta G_n(U = 0) + |e|U \tag{1}$$

The free energy of each adsorbed species can be obtained by correcting the calculated electronic energies using the following method:

$$\Delta G = \Delta E + \Delta ZPE + T\Delta S \tag{2}$$

where G is the free energy, ΔE is the electronic energy of the species from the DFT calculation, T is the temperature and S is the entropy; zero-point energies (ZPE) of adsorbed species have been calculated from frequencies obtained within the harmonic oscillator approximation.

The transition state structures are searched by the nudged elastic band (NEB) method. And they have only one imaginary frequency through the frequency calculations.

3. Results and discussion

3.1 Geometrical and electronic structures of the model

The $Cu_{32}O_8$ bulk comes from our another work that simulated the oxygen desorption progress from bulk CuO to Cu (more details can be found in the ESI†). As shown in Fig. 1a, $Cu_{32}O_8$ bulk is an ordered periodic structure that can be regarded as a combination of Cu_8O_8 phase and Cu_{24} phase. This special structure makes it possible to provide different active sites. By comparing the structures of three different facets ((100), (010), and (111)) (Fig. S7†), we confirm that the (100) facet could expose Cu sites with different chemical valence on the surface. Then we cleave and build the $Cu_{32}O_8(100)$ slab model with vacuum. Fig. 1b shows the optimized $Cu_{32}O_8(100)$ slab, where the Cu atoms with different coordination environments on the top surface are marked as Cu1, Cu2, and Cu3, respectively. The Bader charge analysis for the representative Cu atoms reveals that the charges of the Cu1 atom, Cu2 atom and Cu3 atom are +0.5, 0.0 and +0.2, respectively. In addition, it is indicated that the Cu1 atom has a similar Bader charge value to that of the coordinatively unsaturated Cu atom on the Cu_2O (111) surface. Meanwhile, it can be seen that the Cu2 atoms connect only with other Cu atoms, which is the same as the metallic Cu atoms. This demonstrated that the Cu1 atom and the Cu2 atom have the characteristic property of the Cu^+ and Cu^0 sites, respectively. Besides, the Cu3 atoms with +0.2 charge can also help to

stabilize some intermediates but they are not suitable adsorption sites in the discussion below (Fig. S6†). Our calculations focus on the Cu1 and Cu2 atoms. And we refer to Cu1 atoms and Cu2 atoms by Cu^+ sites and Cu^0 sites in the following discussion. Furthermore, the projected density of states (DOS) result (Fig. S1†) also approves that the Cu1 atom as the Cu^+ site has a larger coordination range than the Cu2 atom as the Cu^0 site. Therefore, the $Cu_{32}O_8(100)$ surface with the adjacent Cu^+ and Cu^0 sites could be used to simulate the Cu based electrocatalysts with the mixed copper states, which can be prepared through electrochemical repeated oxidation-reduction of copper or solution reduction of Cu oxides. It is suitable to be applied to probe the role of Cu^0 and Cu^+ sites in C_2 product formation from the CO_2RR. We also compared the characteristic distance between the Cu atoms. The distance between Cu1 and the adjacent Cu2 atom is similar to that between two Cu atoms on the Cu_2O (111) surface and longer than that on Cu (111) (Fig. S2†).

3.2 Adsorption of CO

Since CO has been widely recognized as a key intermediate to form C_2 products, and also an important reactant of C–C coupling reaction, it is reasonable to investigate the reaction mechanisms upon CO formation *via* the $2e^-$ reduction process of CO_2.[42] Herein, the calculation starts from the adsorption of CO on the Cu^+ site and Cu^0 site, and then the further process towards the final C_2 products, ethanol and ethylene.

The adsorption of CO on the Cu^+ site and Cu^0 site was studied and the result is shown in Fig. 2. It can be seen that the adsorbed CO molecule adopted a similar upright configuration with C atom bonding to the Cu atom on both sites, while the length of the Cu–C bond on the Cu^+ site is 1.809 Å, which is shorter than that on the Cu^0 site (1.885 Å). Meanwhile, our calculations indicate that the *CO adsorption energy on Cu^+ and Cu^0 is −0.47 eV and −0.07 eV, respectively. The relatively low adsorption energy on the Cu^0 site suggests its short residence time but also would be helpful for C–C coupling reaction. And the adsorption energy of CO on Cu^+ sites is 0.40 eV negative
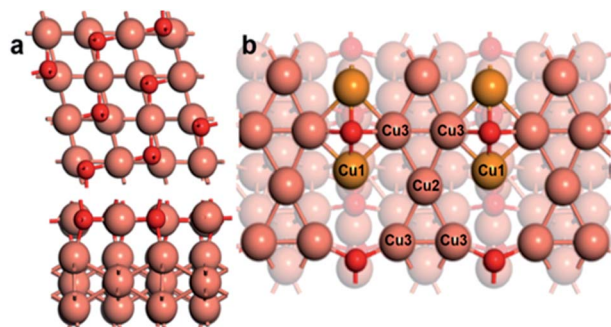

Fig. 1 (a) The optimized structure of $Cu_{32}O_8$ in different views. (b) The optimized $Cu_{32}O_8$ (100) surface. Cu1 atoms are in orange, Cu2 and Cu3 atoms are in orange red, and O atoms are in red.
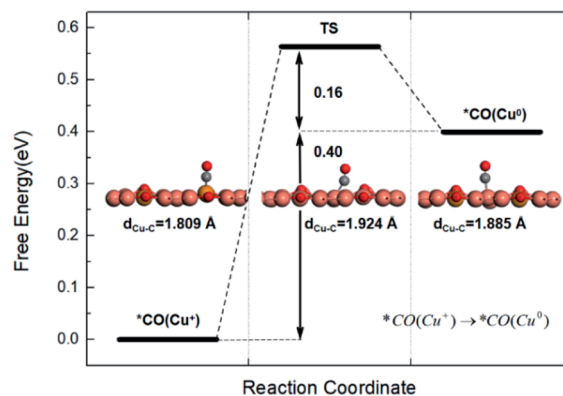

Fig. 2 The migration barrier of CO from the Cu^+ site to the Cu^0 site. The insets are the corresponding adsorption structures of *CO intermediates (Cu^+ atoms are highlighted in orange, other Cu atoms are in brown, O atoms are in red and C atom is in grey).

compared to that on Cu^0 sites, demonstrating that Cu^+ sites are more favourable for CO adsorption. This is in agreement with the previous reports that the coordinatively unsaturated Cu^+ sites have the advantage on stabilizing the CO intermediate.[43] For comparison, we also explore the other possible sites for CO adsorption, such as the Cu3 atom or the bridge sites. As a result, it is demonstrated that CO exclusively tends to adsorb on Cu^+ sites. Therefore, Cu^+ sites enable CO molecular proceeding further reactions on surface due to the inhibition of CO desorption and the stabilization of *CO intermediate.[44]

It is worth noting that though CO is much favourable on Cu^+ sites, CO can also adsorb on the Cu^0 sites in the CO-enriched environments, which makes C–C coupling reactions happen.[32,43] As thus, the migration barrier of *CO from Cu^+ sites to Cu^0 sites was calculated. As shown in Fig. 2, the low barrier of 0.56 eV suggests that this migration process can occur easily at room temperature, since the surmountable barrier is typically below 0.75 eV.[6] Thereafter, in the case of sufficient CO formation, there would form many adjacent *CO pairs on Cu^+ sites to Cu^0 sites as shown in Fig. S3,† which is used as the initial configuration for the further C–C coupling reaction.

3.3 The CO hydrogenation and C–C coupling

After outlining the model systems and the adsorption of CO, we investigate the mechanism of C–C coupling. As invoked in a majority of studies, the dimerization of *CO has naturally become the key step in conversion to multi-carbon products due to the high uphill reaction energy,[45,46] while recently, it is presented that the hydrogenation of CO might be preferable to the dimerization of *CO. Thereby, other C_1 intermediates formed *via* hydrogenation reaction of *CO (R1 and R2) need to be considered.[13,47,48]

$$*CO + (H^+ + e^-) \rightarrow *CHO \qquad (R1)$$

$$*CO + (H^+ + e^-) \rightarrow *COH \qquad (R2)$$

Fig. 3 shows the configuration of *COH and *CHO on the Cu^+/Cu^0 surface. In Fig. 3a, it can be seen that the C atom of *COH forms bonds with three Cu atoms nearby along with the formation of an O–H bond, which makes it closer to the surface as compared to the *CO adsorption configuration. In contrast,

as shown in Fig. 3b, the C atom of *CHO only bonds with the Cu^+ atom. The reaction free energy of *COH formation is 1.06 eV higher than that of *CHO formation (Fig. 4a).

Generally, the differences on connecting ways between the intermediate and surface atoms might determine the tendency of CO hydrogenation. From the configuration of *COH, it is obvious that more available adjacent copper atoms are required to stabilize it due to forming three bonds with the C atom. In addition, considering the further hydrogenation on the O atom of *COH, it would generate H_2O, resulting in the unsaturated C left on the surface, which also demands many available active sites, while for *CHO, the formation of a C–H bond in *CHO could active the C atom and change the upright configuration of the intermediate, which gives the O atom a chance to combine with the surface and form a lying-down configuration.[10] Therefore, the formation of *CHO is preferable on the Cu^+ site in terms of the available bonding atoms.

Furthermore, besides the dimerization of two CO* molecules (R3), the C–C coupling reaction could happen between *CO and *CHO (R4) or CO* and *COH (R5). In some studies, the dimerization reaction of *CHO and *COH is also considered. However, since CO is the major product of CO_2 reduction *via* two steps of proton–electron pair $(H^+ + e^-)$ transfer, it can be supposed that the coverage of *CO is larger than that of *CHO or *COH on the surface. Thereby, it is less likely to have sufficient *CHO or *COH on adjacent sites. As thus, the dimerization reaction of two *CHO or two *COH is not included in this work.

$$*CO + *CO \rightarrow *OCCO \qquad (R3)$$

$$*CO + *CHO \rightarrow *OCCHO \qquad (R4)$$

$$*CO + *COH \rightarrow *OCCOH \qquad (R5)$$

After analysing the possible pathway of coupling, we calculated and compared the free energy of (R3)–(R5) reactions. As shown in Fig. 4a, the coupling reaction between *CO and *COH is the only one exothermic reaction; however, the much higher reaction energy of forming *COH makes this pathway the most difficult to form the C_2 intermediate. In contrast, the formation of a *OCCO intermediate by direct *CO dimerization needs a relatively high reaction energy of 1.23 eV, in accordance with other studies on copper catalysts.[49] In particular, although the coupling reaction between *CO and *CHO is endothermic, the reaction energy is as low as 0.05 eV. Additionally, the barrier of hydrogenation of *CO to *CHO (0.79 eV) is much lower than the reaction energy of CO dimerization (1.23 eV). Moreover, it is indicated that *OCCHO is more stable than *OCCO thermodynamically. Overall, among the three pathways shown in Fig. 4a, the formation of *OCCHO *via* the C–C bond between the hydrogenated intermediate *CHO and *CO is the most favourable. Furthermore, the transition state for the coupling reaction between *CO and *CHO was studied to obtain the reaction barrier. As shown in Fig. 4b, the *CHO intermediate rotates its O atom to combine with the Cu^+ site, and then couples with *CO to form a C–C bond. The energy barrier of this process is
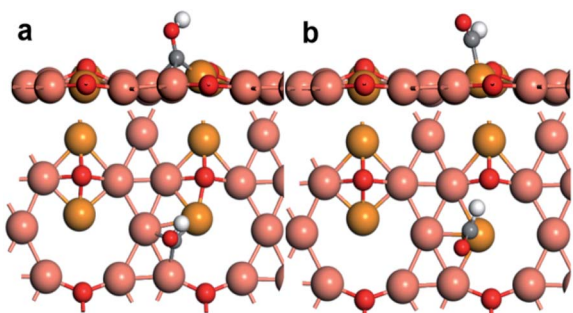

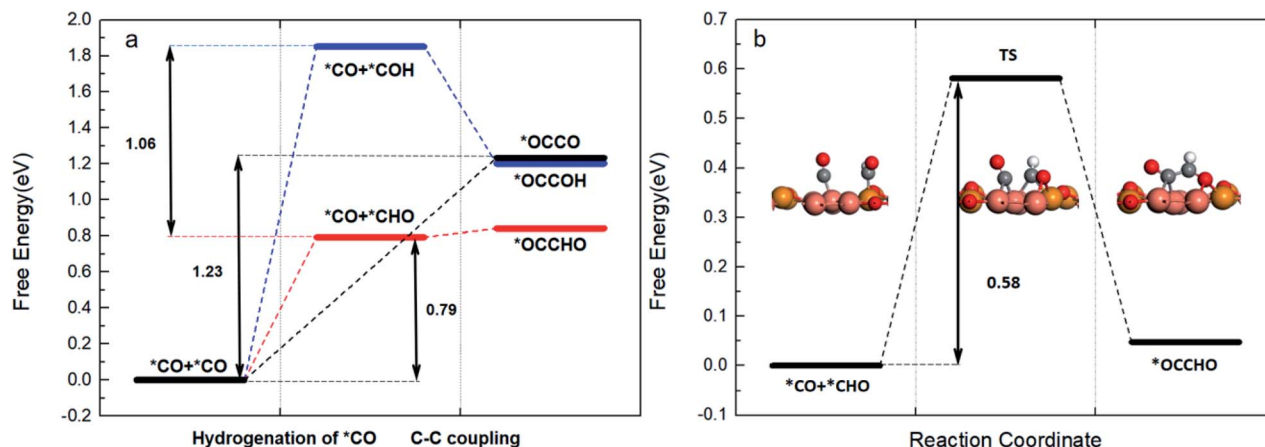**Fig. 3** The configuration of (a) *COH and (b) *CHO on the Cu^+/Cu^0 surface.

Fig. 4 (a) Free energy profiles for different C−C coupling ways. (b) Free energy profile for the coupling of *CO and *CHO intermediates. The insets are the corresponding structures of reaction intermediates.

0.58 eV, which is also easily surmountable at room temperature. In consequence, according to the above results, it is demonstrated that the formation of the *CHO intermediate is a potential limiting step for producing a C_2 intermediate *OCCHO.

The stability of the *OCCO intermediate has relevance with the relative position of Cu atoms connected with C atoms. It is reported that the reaction energy of *CO dimerization on the Cu(100) facet (0.21 eV) is lower than that on the Cu(111) facet (1.24 eV) at 0 V potential.[42,50] Head-Gordon *et al.* proposed that this may be attributed to the square symmetry of Cu(100), where C atoms adsorb on bridge sites and C−C bond length is appropriate, while the relatively high reaction energy of *CO dimerization on our surface (1.23 eV) is very similar to that on Cu (111). This may because the Cu^0 sites share a hexagonal symmetry similar to Cu (111). And the low coordinate state of Cu^+ sites also makes the CO dimer form a less stable geometry. Under this condition, CO dimerization is inhibited by high reaction energy and let the production of hydrogenation intermediates become more competitive. These considerations, along with the relative position of Cu^+ and Cu^0, lead to the formation of *CHO and result in *OCCHO as the final coupling product.

The formation of *OCCHO and *OCCOH has been discussed around potential dependence,[51] pH dependence[52,53] and facet dependence[54–56] and our results suggest the relevance with the Cu oxidation state. In contrast to regular arranged pure Cu surfaces, the Cu^+/Cu^0 arrangement prompts Cu^+ to exert its catalytic properties of stabilizing *CO and converting it into *CHO, and the C−C coupling could climb a lower barrier through the *CO and *CHO pathway. As a result, the presence of the Cu^+/Cu^0 state and relative position of Cu^+ and Cu^0 sites affect the stability of different intermediates, leading to this asymmetric C−C coupling.

3.4 C_2 product formation and the ethanol selectivity

After the *OCCHO formation, we studied the further reduction to the C_2 products, ethanol and ethylene. The plausible

mechanistic steps of C_2 product formation are computationally explored with considering the various hydrogenated intermediates on our surface. The structure of each step is calculated after the structure of the last step is determined. Shown in Fig. 5, the most favourable reduction pathway to ethanol is coloured in blue, whereas less favourable intermediates are displayed in red at each stage of the reaction. Besides, to figure out the key step apart for ethylene, the pathway to ethylene is coloured in green.

Throughout the entire diagram in Fig. 5, we find the reduction after *OCCHO formation is a downhill to the ethanol formation (the configuration of intermediates on the main pathway is in Fig. S4†). The later reduction pathway leading to ethanol is thermodynamically favourable, and the potential-limiting step doesn't exist in post C−C coupling steps, which are commensurate with the conclusions in the literature.[50]

The first step of *OCCHO reduction adds one H atom on the C atom of the CHO part to form *OCCH_2O, and the less favourable intermediates (*OCCHOH and *HOCCHO) on this step both get the H atom on the O atom. Then, the next
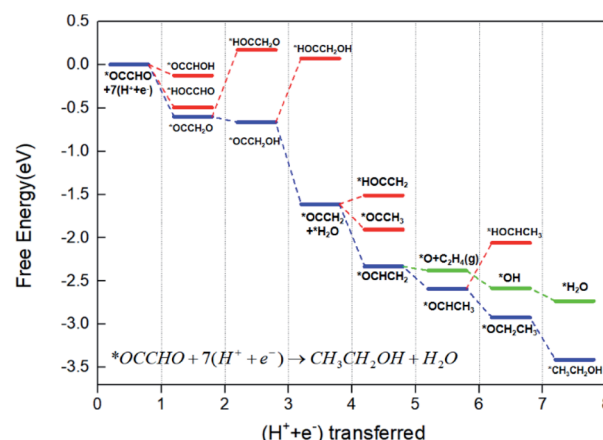

Fig. 5 Free energy profiles for the later reduction of *OCCHO to ethanol.

hydrogenation step of *OCCH$_2$O will be inclined to form *OCCH$_2$OH instead of *HOCCH$_2$O, and the H atom prefers bonding with the O atom on the CH$_2$O part. Further hydrogenation of *OCCH$_2$OH through its O atom will result in *OCCH$_2$ with a H$_2$O molecule left on the surface, which can be removed by electroreduction through a reaction energy of 0.63 eV. The first three (H$^+$ + e$^-$) steps convert *OCCHO to *OCCH$_2$ and the hydrogenation happens only on the α-C side. Through this pathway, the O–H bond formation and the dehydration step happen after the C atom has been occupied by H atoms, which leads to the conversion to *OCHCH$_2$. And this hydrogenation on the α-C side may be due to the asymmetric coupling and our different environment of Cu$^+$/Cu^0 sites.

Then, the key oxygen-bound intermediate *OCHCH$_2$ which divides the formation pathway of ethanol and ethylene forms in the next (H$^+$ + e$^-$) step. Discussion around the determinants of the C$_2$ product selectivity hasn't come to a common conclusion, but *OCHCH$_2$ surely gets more attention as the critical selectivity determining intermediate (SDI) on the pathway.[50,57–59] As shown in Fig. 6, once the C–O bond of *OCHCH$_2$ is broken, C$_2$H$_4$ would generate and leave the *O alone on the surface. After *O hydrogenates to *H$_2$O, the whole pathway to ethylene completes. On the other pathway, it could produce *OCHCH$_3$, which has been detected as the precursor of ethanol formation.[60,61] As the hydrogenation reaction proceeds, the final product comes to ethanol. Our calculation suggests that the formation of *OCHCH$_3$ is 0.21 eV stable compared to *O + C$_2$H$_4$(g) on free energy. Thus, the protonation of α-C to form *OCHCH$_3$ intermediate is thermodynamically favoured compared to the cleavage of the C–O bond to form C$_2$H$_4$, which means the generation of ethanol.

Several studies have tried to find the descriptor for selectivity between ethanol and ethylene on pure Cu or oxide-derived Cu electrocatalysts. Calle-Vallejo and co-workers pointed that the adsorption energy of acetaldehyde (CH$_3$CHO) and the *O adsorption energy may be the descriptor.[42] Their analysis suggested that actives with large adsorption energy of acetaldehyde would perform well on enhancing ethanol selectivity and the active sites bind *O weakly could inhibit the pathway to ethylene.

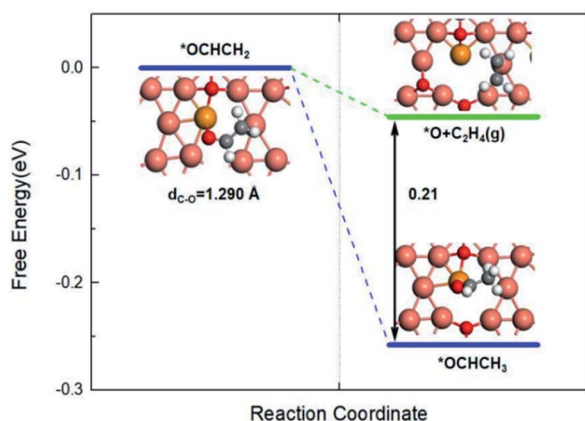Our calculation indicates that the adsorption energy of acetaldehyde on Cu$^+$ sites is −0.39 eV. This relatively high adsorption energy suggests that the low coordinated Cu$^+$ site binds acetaldehyde strong enough to prevent its desorption once formed, inclining the selectivity toward ethanol production. Besides, the configurations in Fig. 6 suggest that *O can only adsorb on the adjacent triple site of the Cu^0 part, which leads to the instability of *O. In fact, we cannot find the suitable and stable structure for *O on the hollow site between Cu$^+$ and Cu^0 during the optimization calculations, which means that the long distance between Cu$^+$ and Cu^0 cannot provide suitable sites let alone the single Cu$^+$ atom. Gong et al.[59] also pointed that the triple site performs bad in stabilizing the newly formed *O after C–O cleavage. The *O adsorption is unstable due to the configuration of Cu$^+$/Cu^0 sites, which limits ethylene production.

In addition, the C–O bond length in adsorbed *OCHCH$_2$ can be a simple descriptor. The C–O length of the *OCHCH$_2$ on our Cu$^+$ site is 1.290 Å (another configuration of *OCHCH$_2$ with the O atom combining to the Cu^0 site is 1.322 Å, Fig. S5†), which is relatively short compared to the length (1.296 Å–1.322 Å) on different copper facets listed in the literature.[59] This also suggests that the C–O bond is hard to break once combined to the Cu$^+$ site and the ethylene pathway is inhibited. Thus, the selectivity for ethanol of our adjacent Cu$^+$/Cu^0 sites also comes from the promotion of stability for the critical intermediate and the inhibition of intermediates with more bonding demand.

4 Conclusions

In summary, we have built a surface consisting of adjacent Cu$^+$ and Cu^0 sites as a partially reduced Cu$_2$O electrocatalyst for the CO$_2$RR with the selectivity for ethanol. Our results suggest that CO tends to adsorb on the Cu$^+$ sites only and also can migrate to the Cu^0 site, and the presence of Cu$^+$ can stabilize the CO intermediate and ensure further CO reduction to occur. The hydrogenation of *CO can be the key step before C–C coupling and the coupling between *CO and *CHO has an advantage over the dimerization of *CO due to the different state and relatively long distance between the Cu$^+$ and Cu^0 sites. In addition, the oxygen-bound intermediate *OCHCH$_2$ divides the pathway of ethanol and ethylene. The low coordinated Cu$^+$ site could maintain the C–O bond of *OCHCH$_2$ and stabilize the *OCHCH$_3$ intermediate. And the configuration of the Cu$^+$/Cu^0 surface results in weak *O binding, which inhibits the ethylene pathway. Above all, our calculations on adjacent Cu$^+$/Cu^0 sites explored the mechanism of the CO$_2$RR by discussing the process of the hydrogenation of CO, C–C coupling and *OCHCH$_2$ reduction and claimed the effect of Cu oxidation state. We hope this study provides insightful guidelines for the design of CO and CO$_2$ reduction active sites with enhanced ethanol selectivity.

Conflicts of interest

There are no conflicts to declare.

Fig. 6 Free energy profiles for the bifurcation pathway of *OCHCH$_2$ on Cu$^+$/Cu^0 sites. The insets are the corresponding structures.

Acknowledgements

Notes and references

1 J. P. Gattuso, A. Magnan, R. Bille, W. W. Cheung, E. L. Howes, F. Joos, D. Allemand, L. Bopp, S. R. Cooley, C. M. Eakin, O. Hoegh-Guldberg, R. P. Kelly, H. O. Portner, A. D. Rogers, J. M. Baxter, D. Laffoley, D. Osborn, A. Rankovic, J. Rochette, U. R. Sumaila, S. Treyer and C. Turley, *Science*, 2015, **349**, aac4722.

2 S. Solomon, G.-K. Plattner, R. Knutti and P. Friedlingstein, *Proc. Natl. Acad. Sci. U. S. A.*, 2008, **106**, 1704–1709.

3 H.-R. M. Jhong, S. Ma and P. J. A. Kenis, *Curr. Opin. Chem. Eng.*, 2013, **2**, 191–199.

4 K. Jiang, S. Siahrostami, A. J. Akey, Y. Li, Z. Lu, J. Lattimer, Y. Hu, C. Stokes, M. Gangishetty, G. Chen, Y. Zhou, W. Hill, W.-B. Cai, D. Bell, K. Chan, J. K. Nørskov, Y. Cui and H. Wang, *Chem*, 2017, **3**, 950–960.

5 J. B. Greenblatt, D. J. Miller, J. W. Ager, F. A. Houle and I. D. Sharp, *Joule*, 2018, **2**, 381–420.

6 S. Nitopi, E. Bertheussen, S. B. Scott, X. Liu, A. K. Engstfeld, S. Horch, B. Seger, I. E. L. Stephens, K. Chan, C. Hahn, J. K. Norskov, T. F. Jaramillo and I. Chorkendorff, *Chem. Rev.*, 2019, **119**, 7610–7672.

7 H. Zhang, J. Li, M.-J. Cheng and Q. Lu, *ACS Catal.*, 2018, **9**, 49–65.

8 S. Hanselman, M. T. M. Koper and F. Calle-Vallejo, *ACS Energy Lett.*, 2018, **3**, 1062–1067.

9 K. P. Kuhl, E. R. Cave, D. N. Abram and T. F. Jaramillo, *Energy Environ. Sci.*, 2012, **5**, 7050–7059.

10 K. J. P. Schouten, Y. Kwon, C. J. M. van der Ham, Z. Qin and M. T. M. Koper, *Chem. Sci.*, 2011, **2**, 1902–1909.

11 E. L. Clark, C. Hahn, T. F. Jaramillo and A. T. Bell, *J. Am. Chem. Soc.*, 2017, **139**, 15848–15857.

12 F. Dattila, R. García-Muelas and N. López, *ACS Energy Lett.*, 2020, **5**, 3176–3184.

13 X. Yan, C. Chen, Y. Wu, S. Liu, Y. Chen, R. Feng, J. Zhang and B. Han, *Chem. Sci.*, 2021, **12**, 6638–6645.

14 W. Luo, X. Nie, M. J. Janik and A. Asthagiri, *ACS Catal.*, 2015, **6**, 219–229.

15 L. Zhang, M. Li, S. Zhang, X. Cao, J. Bo, X. Zhu, J. Han, Q. Ge and H. Wang, *Catal. Today*, 2021, **365**, 348–356.

16 L. R. L. Ting, O. Piqué, S. Y. Lim, M. Tanhaei, F. Calle-Vallejo and B. S. Yeo, *ACS Catal.*, 2020, **10**, 4059–4069.

17 S. Ishimaru, R. Shiratsuchi and G. Nogami, *J. Electrochem. Soc.*, 2000, **147**, 1864–1867.

18 L. Xiong, X. Zhang, H. Yuan, J. Wang, X. Yuan, Y. Lian, H. Jin, H. Sun, Z. Deng, D. Wang, J. Hu, H. Hu, J. Choi, J. Li, Y. Chen, J. Zhong, J. Guo, M. H. Rummerli, L. Xu and Y. Peng, *Angew. Chem., Int. Ed.*, 2021, **60**, 2508–2518.

19 X. Wang, J. F. de Araujo, W. Ju, A. Bagger, H. Schmies, S. Kuhl, J. Rossmeisl and P. Strasser, *Nat. Nanotechnol.*, 2019, **14**, 1063–1070.

20 X. Yuan, S. Chen, D. Cheng, L. Li, W. Zhu, D. Zhong, Z. J. Zhao, J. Li, T. Wang and J. Gong, *Angew. Chem., Int. Ed.*, 2021, **60**, 15344–15347.

21 Z. Tang, E. Nishiwaki, K. E. Fritz, T. Hanrath and J. Suntivich, *ACS Appl. Mater. Interfaces*, 2021, **13**, 14050–14055.

22 D. Kim, S. Lee, J. D. Ocon, B. Jeong, J. K. Lee and J. Lee, *Phys. Chem. Chem. Phys.*, 2015, **17**, 824–830.

23 P. P. Yang, X. L. Zhang, F. Y. Gao, Y. R. Zheng, Z. Z. Niu, X. Yu, R. Liu, Z. Z. Wu, S. Qin, L. P. Chi, Y. Duan, T. Ma, X. S. Zheng, J. F. Zhu, H. J. Wang, M. R. Gao and S. H. Yu, *J. Am. Chem. Soc.*, 2020, **142**, 6400–6408.

24 C. W. Li, J. Ciston and M. W. Kanan, *Nature*, 2014, **508**, 504–507.

25 S. C. Lin, C. C. Chang, S. Y. Chiu, H. T. Pai, T. Y. Liao, C. S. Hsu, W. H. Chiang, M. K. Tsai and H. M. Chen, *Nat. Commun.*, 2020, **11**, 3525.

26 H. Xiao, W. A. Goddard, 3rd, T. Cheng and Y. Liu, *Proc. Natl. Acad. Sci. U. S. A.*, 2017, **114**, 6685–6688.

27 G. Y. Duan, X. Q. Li, G. R. Ding, L. J. Han, B. H. Xu and S. J. Zhang, *Angew. Chem., Int. Ed.*, 2022, **61**, e202110657.

28 X. Yuan, S. Chen, D. Cheng, L. Li, W. Zhu, D. Zhong, Z. J. Zhao, J. Li, T. Wang and J. Gong, *Angewandte Chemie International Edition*, 2021, **60**, 15344–15347.

29 H. Xiao, T. Cheng, W. A. Goddard, 3rd and R. Sundararaman, *J. Am. Chem. Soc.*, 2016, **138**, 483–486.

30 C. C. Chang, E. Y. Li and M. K. Tsai, *Phys. Chem. Chem. Phys.*, 2018, **20**, 16906–16909.

31 S. Lee, D. Kim and J. Lee, *Angew. Chem., Int. Ed.*, 2015, **54**, 14701–14705.

32 X. Bai, Q. Li, L. Shi, X. Niu, C. Ling and J. Wang, *Small*, 2020, **16**, e1901981.

33 L. Li, H. Wang, J. Han, X. Zhu and Q. Ge, *J. Chem. Phys.*, 2020, **152**, 054709.

34 G. Kresse and J. Furthmuller, *Phys. Rev. B: Condens. Matter Mater. Phys.*, 1996, **54**, 11169–11186.

35 G. Kresse and J. Furthmuller, *Comput. Mater. Sci.*, 1996, **6**, 15–50.

36 G. Kresse and J. Hafner, *Phys. Rev. B: Condens. Matter Mater. Phys.*, 1993, **47**, 558–561.

37 G. Kresse and J. Hafner, *Phys. Rev. B: Condens. Matter Mater. Phys.*, 1994, **49**, 14251–14269.

38 J. P. Perdew, J. A. Chevary, S. H. Vosko, K. A. Jackson, M. R. Pederson, D. J. Singh and C. Fiolhais, *Phys. Rev. B: Condens. Matter Mater. Phys.*, 1992, **46**, 6671–6687.

39 A. K. Mishra, A. Roldan and N. H. d. Leeuw, *J. Phys. Chem. C*, 2016, **120**, 2198–2214.

40 J. K. Nørskov, J. Rossmeisl, A. Logadottir and L. Lindqvist, *J. Phys. Chem. C*, 2004, **108**, 17886–17892.

41 A. Bagger, L. Arnarson, M. H. Hansen, E. Spohr and J. Rossmeisl, *J. Am. Chem. Soc.*, 2019, **141**, 1506–1514.

42 O. Piqué, F. Viñes, F. Illas and F. Calle-Vallejo, *ACS Catal.*, 2020, **10**, 10488–10494.

43 J. Yu, M. Yang, J. Zhang, Q. Ge, A. Zimina, T. Pruessmann, L. Zheng, J.-D. Grunwaldt and J. Sun, *ACS Catal.*, 2020, **10**, 14694–14706.

44 M. Le, M. Ren, Z. Zhang, P. T. Sprunger, R. L. Kurtz and J. C. Flake, *J. Electrochem. Soc.*, 2011, 158.

45 R. B. Sandberg, J. H. Montoya, K. Chan and J. K. Nørskov, *Surf. Sci.*, 2016, **654**, 56–62.

46 J. H. Montoya, C. Shi, K. Chan and J. K. Norskov, *J. Phys. Chem. Lett.*, 2015, **6**, 2032–2037.

47 W. Ma, S. Xie, T. Liu, Q. Fan, J. Ye, F. Sun, Z. Jiang, Q. Zhang, J. Cheng and Y. Wang, *Nat. Catal.*, 2020, **3**, 478–487.

48 J. H. Montoya, A. A. Peterson and J. K. Nørskov, *ChemCatChem*, 2013, **5**, 737–742.

49 H. Li, Y. Li, M. T. Koper and F. Calle-Vallejo, *J. Am. Chem. Soc.*, 2014, **136**, 15694–15701.

50 A. J. Garza, A. T. Bell and M. Head-Gordon, *ACS Catal.*, 2018, **8**, 1490–1499.

51 E. Perez-Gallent, G. Marcandalli, M. C. Figueiredo, F. Calle-Vallejo and M. T. M. Koper, *J. Am. Chem. Soc.*, 2017, **139**, 16412–16419.

52 F. S. Roberts, K. P. Kuhl and A. Nilsson, *ChemCatChem*, 2016, **8**, 1119–1124.

53 K. J. P. Schouten, E. Pérez Gallent and M. T. M. Koper, *J. Electroanal. Chem.*, 2014, **716**, 53–57.

54 W. J. Durand, A. A. Peterson, F. Studt, F. Abild-Pedersen and J. K. Nørskov, *Surf. Sci.*, 2011, **605**, 1354–1359.

55 R. M. Aran-Ais, D. Gao and B. Roldan Cuenya, *Acc. Chem. Res.*, 2018, **51**, 2906–2917.

56 K. J. Schouten, Z. Qin, E. Perez Gallent and M. T. Koper, *J. Am. Chem. Soc.*, 2012, **134**, 9864–9867.

57 O. Pique, Q. H. Low, A. D. Handoko, B. S. Yeo and F. Calle-Vallejo, *Angew. Chem., Int. Ed.*, 2021, **60**, 10784–10790.

58 X. Zhi, A. Vasileff, Y. Zheng, Y. Jiao and S.-Z. Qiao, *Energy Environ. Sci.*, 2021, **14**, 3912–3930.

59 D. Cheng, Z. J. Zhao, G. Zhang, P. Yang, L. Li, H. Gao, S. Liu, X. Chang, S. Chen, T. Wang, G. A. Ozin, Z. Liu and J. Gong, *Nat. Commun.*, 2021, **12**, 395.

60 I. Ledezma-Yanez, E. P. Gallent, M. T. M. Koper and F. Calle-Vallejo, *Catal. Today*, 2016, **262**, 90–94.

61 E. Bertheussen, A. Verdaguer-Casadevall, D. Ravasio, J. H. Montoya, D. B. Trimarco, C. Roy, S. Meier, J. Wendland, J. K. Norskov, I. E. Stephens and I. Chorkendorff, *Angew. Chem., Int. Ed.*, 2016, **55**, 1450–1454.